Maxwell-Bloch modeling of an x-ray-pulse amplification in a one-dimensional photonic crystal

O. Peyrusse*
Aix-Marseille Université, CNRS UMR 7345, PIIM Marseille, France

P. Jonnard and J.-M. André
Sorbonne Université, Faculté des Sciences et Ingénierie, UMR CNRS, Laboratoire de Chimie Physique – Matière et Rayonnemment, 4 Place Jussieu, F-75252 Paris Cedex 05, France

(Received 2 December 2020; accepted 19 March 2021; published 9 April 2021)

We present an implementation of the Maxwell-Bloch formalism for the study of x-ray emission dynamics from periodic multilayer materials whether they are artificial or natural. The treatment is based on a direct finite-difference time-domain solution of Maxwell equations combined with Bloch equations incorporating a random spontaneous emission noise. Besides periodicity of the material, the treatment distinguishes between two kinds of layers, those being active (or resonant) and those being off-resonance. The numerical model is applied to the problem of $K\alpha$ emission in multilayer materials where the population inversion could be created by fast inner-shell photoionization by an x-ray free-electron laser. Specificities of the resulting amplified fluorescence in conditions of Bragg diffraction are illustrated by numerical simulations. The corresponding pulses could be used for specific investigations of nonlinear interaction of x rays with matter.

DOI: 10.1103/PhysRevA.103.043508

I. INTRODUCTION

Nonlinear optical devices (NLO) have been a vivid subject of study for their numerous applications. Within the domain of x-ray quantum optics [1,2], the field of nonlinear x-ray (NLX-ray) devices is much less explored since, compared with the optical range, the control of x rays is more difficult. The simplest NLX-ray device is an ensemble of 2,3-level atoms for which different studies of pulse propagation and of several nonlinear effects have been reported (see, for instance, [3]). Other typical NLX-ray devices are multilayer materials which are used in x-ray optics. Short and ultraintense x-ray sources such as x-ray free-electron lasers (XFELs) are pushing the boundaries of the response to x rays in such devices. Besides this, it has been proven that XFEL sources have the potential to create large population inversions in gases [4], clusters [5], solids [6–8], and liquids [9], resulting in the creation of an x-ray amplifying medium. These approaches based on lasing in atomic media have an important potential to obtain useful short and coherent x-ray pulses. Indeed, high-quality short pulses going beyond the inherent defaults of SASE XFEL pulses (of spiky and chaotic nature) are a prerequisite for future investigations concerning x-ray quantum optics, x-ray scattering, precision spectroscopy, or pump-probe experiments requiring a coherent probe. Compared with conventional lasers, these approaches suffer from the lack of a resonator to extract most of the energy stored in an inverted medium. In other words, there remains the problem of realizing x-ray feedback to achieve laser oscillation in the x-ray range. Hence a work going in that direction has recently been reported [10]. In this reported work a classical multipass meter-sized laser cavity has been set up., the x-ray lasing medium being a liquid jet pumped by an XFEL. Besides this, within the context of XFEL excitation and to extract energy stored in an inverted medium, the idea of using the phenomenon of collective spontaneous decay or superradiance (named also superfluorescence) has been discussed and explored [11] but in the visible range. Independently, it has been suggested that a laser action in the x-ray range can be provided by Bragg reflection inside a natural crystal or inside an artificial multilayer material [12–14]. Note that in the first case, the Bragg condition is constrained by the crystal periodicity.

The goal of this paper is to study numerically x-ray feedback under Bragg conditions as well as pulse propagation in one-dimensional (1D) photonic crystals in which a population inversion has been initiated by some external source. Here we go beyond a description where the multilayer is simply described by the complex refractive index of each layer [14]. Even when the complex part of the refractive index is negative (i.e., amplifying), such a description is basically linear and corresponds to the linear phase of the interaction of an x-ray pulse with the material. Note that this remark concerns the *active* layers only. *Passive* layers, for which no resonant response is expected, can still be described by a complex refractive index. This defines the specificity of our description, which mixes a nonlinear treatment and a linear treatment, i.e., more precisely, using a Maxwell-Bloch (MB) formalism or a standard formalism, depending on the kind of layer (active or passive).

In this paper we consider a large number of photons in the radiation modes. As a consequence, quantum fluctuations are neglected and the electromagnetic (EM) field is described by Maxwell equations. In the absence of an external source, one shortcoming of the MB description is that there is no

*olivier.peyrusse@univ-amu.fr

mechanism for spontaneous emission. It is well known that this problem can be overcome by adding a phenomenological fluctuating polarization source that simulates spontaneous emission (although this approach has some drawbacks, as discussed below). Compared with many calculations of x-ray lasing in gas or plasmas (see, for instance, Refs. [15–18]), short spatial scales involved in this multilayer context do not permit the use of the *slowly varying envelope approximation* so that basic Maxwell equations have to be solved directly. This is done here using the so-called finite-difference time-domain (FDTD) method [19]. Furthermore, in this multilayer (or 1D photonic crystal) context we consider a 1D plane geometry. Also, we consider only two levels resonantly coupled to the EM field in the MB system. Other levels are taken into account through relaxation and source terms in the equations governing populations of these two levels.

In the following we present the physical model used here (Sec. II), underlining the specific choices made for considering 1D photonic crystals in the x-ray range. Then we turn to a discussion of simulation results in Sec. III. Physical situations considered here evolve gradually from very formal situations to situations close to actual experimental conditions. More precisely, we begin with a situation intended at testing the FDTD implementation in the context of the fluorescence of a multilayer. Here there is no solving of the Bloch equations; instead, a source of emission is assumed in each cell (Sec. III A). Then, after these considerations of the validity of the FDTD implementation, we turn to MB calculations and we consider in detail the problem of an x-ray pulse propagation in a particular stack of bilayers (Mg/Co) in which an initial population inversion is supposed (Sec. III B). After this, one considers the self-emission of such a stack, i.e., as initiated by spontaneous emission (Sec. III C). Finally, we turn to situations where an XFEL source is used for pumping (i.e., for creating the population inversion) either a multilayer (such as a bi-layer (Mg/Co) stack Sec. III D) or a simple Ni crystal (Sec. III E). Section IV summarizes these results.

II. THEORETICAL APPROACH

A. Basic equations

As said in the Introduction, the medium considered here consists of alternating *active* and *passive* materials with a given periodicity—*active* in the sense of resonantly coupled with the EM field at some pulsation ω_o and *passive* if there is no resonant coupling. The two first basic equations of our approach are the Faraday and the Ampere laws, respectively written in the form (SI units)

$$\vec{\nabla} \times \vec{E} = -\partial_t \vec{B}, \tag{1}$$

$$\frac{1}{\mu_o}\vec{\nabla} \times \vec{B} = \epsilon_o \epsilon_r \partial_t \vec{E} + \vec{j}, \tag{2}$$

$\vec{E}$, $\vec{B}$ are the electric and the magnetic fields (real quantities), respectively. ϵ_o, μ_o are the vacuum permittivity and permeability, respectively. ϵ_r is the relative permittivity (here time independent), and $\vec{j}$ is the local current induced by the EM field. In a linear material, i.e., here in a *passive* layer, $\vec{j} = \sigma \vec{E}$, where σ is the electric conductivity. At pulsation ω_o, adiabatic

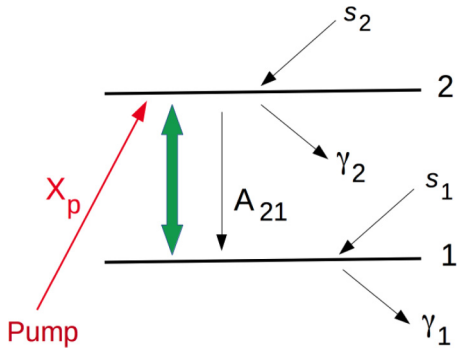

FIG. 1. Level scheme with the associated source or loss rates. The thick line with two arrows represents the Maxwell-Bloch coupling.

properties of the material (in the sense of an instantaneous response to the applied field) are included in the *real* quantities ϵ_r and σ. If the material is described by a complex refractive index of the form (as in current data tables [20,21])

$$n = (1 - \delta) - i\beta,$$

there is an equivalence between the conductivity approach and the refractive index in the sense that

$$\epsilon_r = (1 - \delta)^2 - \beta^2, \quad \sigma = 2(1 - \delta)\beta\omega_o\epsilon_o.$$

In a so-called *active* medium such as the so-called *active* layers, one has $\vec{j} = \partial_t \vec{\mathcal{P}}$, where $\vec{\mathcal{P}}$ is the macroscopic polarization. Considering two levels coupled by the EM field, the macroscopic polarization is defined as the trace of the operator $N\rho\vec{d}$, where N is the density of polarizable atoms, $\vec{d}$ is the atomic dipole, and ρ is the density matrix. Hence

$$\vec{\mathcal{P}} = 2N\mathrm{Re}[\rho_{21}]\vec{d}. \tag{3}$$

The nondiagonal matrix element of the density matrix ρ_{21} is a complex number as the diagonal elements ρ_{11}, ρ_{22} are real quantities. These matrix elements are obtained from the following evolution of the density matrix (Liouville equation) $i\hbar\partial_t = [H, \rho]$ + relaxation and source terms. Here, assuming a polarization along axis Ox, the Hamiltonian H has the form $H = \begin{pmatrix} \epsilon_1 & -dE_x \\ -dE_x & \epsilon_2 \end{pmatrix}$, where both E_x and $d = \langle 1|d_x|2\rangle$ are real quantities. $\epsilon_{1,2}$ are the energies of the coupled levels. Hereafter, $\hbar\omega_o = \epsilon_2 - \epsilon_1$. The level scheme of the problem is depicted in Fig. 1.

In a warm or hot medium, γ_1, γ_2 are the rates (in s^{-1}) of the collisional, radiative, and Auger processes, which depopulate states, except stimulated emission and spontaneous emission. A_{21} is the spontaneous emission rate. Here s_1, s_2 are the possible population fluxes due to all processes, except absorption between states 1 and 2. $\gamma_{1,2}$ and $s_{1,2}$ may involve other levels in the system. We define $\gamma_\perp = \frac{1}{2}(\gamma_1 + \gamma_2) + \gamma_\phi$ so that $1/\gamma_\perp$ can be seen as the lifetime of the coherent superposition of states $|1\rangle$ and $|2\rangle$. In principle, γ_ϕ is supposed to be the rate of events perturbing the wave function without inducing a decay of eigenstates. Hereafter, we called populations of states 1 and 2 the macroscopic quantities $N_1 = N\rho_{11}$, $N_2 = N\rho_{22}$, respectively.

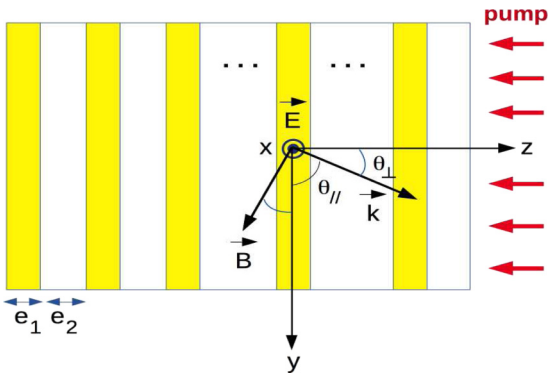

FIG. 2. Sketch of a stack of bilayers made of one *active* element (yellow) and of one *passive* element. On one side the stack is submitted to a source of excitation (the pump). Propagation of the emerging radiation is described by Maxwell equations at some frequency (which is resonant for the active layers). In active layers, the response is described by the Bloch equations, while in passive layers, the response is given by the refractive index.

In an active layer, the set of equations to be solved locally for the populations N_1, N_2 and for the macroscopic coherence $P = N\rho_{21}$ is then

$$\partial_t N_1 = -\frac{2}{\hbar} d E_x \mathrm{Im}[P] + s_1 - \gamma_1 N_1 + A_{21} N_2, \tag{4}$$

$$\partial_t N_2 = \frac{2}{\hbar} d E_x \mathrm{Im}[P] + s_2 - \gamma_2 N_2 - A_{21} N_2 + X_p, \tag{5}$$

$$\partial_t P = -i\omega_o P - \gamma_\perp P - i(N_2 - N_1) d E_x + S, \tag{6}$$

where we added in Eq. (5) a pump source term X_p. S is a phenomenological random source modeling the spontaneous emission. In the absence of external incoming radiation, S acts as an energy seed for energy injection in the system. Equations (1)–(6) correspond to our set of Maxwell-Bloch equations where Eqs. (4)–(6) concern the active layers only. In the literature, the name of Maxwell-Bloch [22], or sometimes Maxwell-Schrödinger [15], is often given to the coupling of complex slowly varying *envelopes* of the EM field with the Bloch equations for the density matrix. Here, there is no approximation concerning the field variation both in space and time.

B. Wave equations in a 1D photonic medium at oblique incidence

A sketch of the physical problem is given in Fig. 2. The medium is made of a periodic stack of different materials (at least two different materials). One is the active material (i.e. described by the MB equations), the other(s) is (are) the passive (or linear) material(s), i.e., described by complex refractive indices.

$(\vec{k}, \vec{E}, \vec{B})$ represent a plane wave propagating in the material under the angle $\theta_\perp$. Hereafter we make use of $\theta_\perp$, which is the angle with respect to a direction *perpendicular* to the surface xy while it may be more convenient to use $\theta_{//} = \frac{\pi}{2} - \theta_\perp$. In this geometry, Faraday's law [Eq. (1)] reads

$$\partial_z E_x = -\partial_t B_y, \tag{7}$$

$$\partial_y E_x = \partial_t B_z, \tag{8}$$

while Ampere's law [Eq. (2)] reads

$$-\partial_z B_y + \partial_y B_z = \frac{\epsilon_r}{c^2} \partial_t E_x + \mu_o j_x, \tag{9}$$

where $j_x = \sigma E_x$ is in a *passive* layer. In an *active* layer, $\epsilon_r = 1$ and $j_x = \partial_t \mathcal{P}_x$, $\mathcal{P}_x$ being deduced from Eq. (3), i.e., $\mathcal{P}_x = 2d\mathrm{Re}[P]$. Translating (7), (8), and (9) from the time domain to the frequency domain gives three equations in which E_x has the behavior $E_x \sim \exp(i\omega_o t \pm iky \sin\theta_\perp)$. Eliminating B_z and going back to the time domain ($i\omega_o \to \partial_t$) finally gives the following two equations governing the behavior of a plane wave for an arbitrary oblique incidence in the multilayer material:

$$\partial_z E_x = -\partial_t B_y, \tag{10}$$

$$-\partial_z B_y = \frac{1}{c^2}(\epsilon_r - \sin^2\theta_\perp)\partial_t E_x + \mu_o j_x. \tag{11}$$

To solve these equations, one uses the usual FDTD method [19], namely, a second-order central difference scheme introduced by Yee [23]. Yee's scheme consists in writing the central differences of E_x and B_y, shifted in space by half a cell and in time by half a time step. In our implementation, B is evaluated at the edge of each cell, while E is evaluated at the center. Accordingly, proper boundary conditions for B have to be applied on each side of the multilayer. Considering that the two external layers (on both sides) correspond to the vacuum (refractive index $n = 1$), and in order to remove reflections from these boundaries, we used second-order absorbing boundary conditions (ABCs) [24]. Together with E_x, the quantities N_1, N_2, and P are cell centered and are advanced in time using a Crank-Nicolson scheme.

Concerning the sampling in space, typically at least 20 steps per wavelength are necessary. This involves a subdivision of each layer in much smaller layers of thicknesses Δz. Accordingly, the sampling in time is governed by the Courant limit. More precisely, an inspection of Eq. (11) shows that the front phase velocity is $c/\sqrt{\epsilon_r - \sin^2\theta_\perp}$. Then the time step must be such that

$$\Delta t \leqslant \frac{\Delta z}{c}\sqrt{\epsilon_r - \sin^2\theta_\perp}.$$

C. Incident source – Spontaneous emission

For some applications it may be useful to consider the seeding of the multilayer by some incident external polarized x-ray pulse (see Sec. III B below). Practically, this can be an external source of x rays at ω_o generated independently. Note that we distinguish this potential seeding source at ω_o from another source (not at ω_o) allowing creation of a population inversion. In order to follow an x-ray pulse propagating in one specific direction, the positive z direction, for instance (see Fig. 2), this source at ω_o has to be properly implemented. As usual in FDTD simulations, this is accomplished using a total-field/scattered-field (TFSF) boundary [25] at the point where the source(s) is (are) put. For instance, this source can be placed in the left vacuum cell of our simulation domain. More precisely, one defines both an incident electric field E^{inc} and an incident magnetic field $B^{\mathrm{inc}} = \cos\theta_\perp \sqrt{\epsilon_r} E^{\mathrm{inc}}$ ($\epsilon_r = 1$ in the vacuum). At the location of the source, according to the TFSF method, E must be replaced by $E - E^{\mathrm{inc}}$ in the

discretized evolution of the B field, while B must be replaced by $B + B^{\text{inc}}$ in the discretized evolution of the E field.

Independently of any external source at ω_o, the source of spontaneous emission in Eq. (6) (the term S) can be modeled as a Gaussian white noise following the guidelines of Ref. [16], an approach followed later by others [17,18]. The interest of this approach is that it provides the correct spectral behavior for the field [16]. Here, one starts from the simplified (local) system [see Eqs. (11) and (6)] coupling the electric field and $P = N\rho_{21}$:

$$\frac{dE}{dt} = \alpha \text{Re}\left[\frac{dP}{dt}\right] (\alpha = -2\mu_o c^2 d), \tag{12}$$

$$\frac{dP}{dt} = -i\omega_o P - \gamma P + S, \tag{13}$$

where the noise source S (complex) has the correlation function $\langle S^*(t')S(t)\rangle = F\delta(t'-t)$. The notation $\langle ...\rangle$ is used to represent the statistical ensemble averaging, and F is a constant defined by the following arguments. From the density of the electric field $\frac{\epsilon_o}{2}E^2$, one defines an average power density W which must be equal to the power emitted by spontaneous emission (in one direction) so that

$$W = \frac{d}{dt}\left(\frac{\epsilon_o}{2}\langle E^2\rangle\right) = \frac{1}{4\pi} N_2 A_{21} \hbar\omega_o. \tag{14}$$

From the formal solution of Eq. (12), $E(t) = \alpha \int_{-\infty}^{t} \text{Re}[\frac{dP(t')}{dt'}]dt'$, one gets

$W = \epsilon_o \langle E \frac{dE}{dt}\rangle = \alpha^2 \epsilon_o \int_{-\infty}^{t} \langle \text{Re}[\frac{dP(t')}{dt'}]\text{Re}[\frac{dP(t)}{dt}]\rangle dt'$. Using (13), W becomes

$$W = \frac{\epsilon_o}{4}\alpha^2 \int_{-\infty}^{t} \left(\left\langle \frac{dP^*(t')}{dt'}\frac{dP(t)}{dt}\right\rangle + \left\langle \frac{dP(t')}{dt'}\frac{dP^*(t)}{dt}\right\rangle\right) dt'. \tag{15}$$

From the formal solution of Eq. (13), $P(t) = \int_{-\infty}^{t} S(t')e^{-i\omega_o(t-t')}e^{-\gamma(t-t')}dt'$, it is easy to calculate quantities $\langle ...\rangle$, so that after averaging over one period, calculation of the integrals in (15) gives (since $\omega_o \gg \gamma$) $W = \frac{\epsilon_o}{4}\alpha^2 \frac{F}{2}\frac{\omega_o^2}{\gamma^2}$. Then from relation (14) one gets

$$F(z,t) = \frac{2A_{21}\hbar\omega_o N_2(z,t)}{\alpha^2 \pi \epsilon_o}\frac{\gamma^2}{\omega_o^2}. \tag{16}$$

Practically, over a time step Δt, the noise source term S in Eq. (6) is a random complex number $u + it$ distributed according to the law $\frac{1}{\pi\sigma_S^2}\exp[-(u^2+t^2)/\sigma_S^2]$ with $\sigma_S = \sqrt{F\Delta t}$.

The action of this local phenomenological model of spontaneous emission as set from Eqs. (12) and (13) is to inject a random macroscopic coherence at each point and at each instant. While giving the correct number of photons, a shortcoming of this approach (as discussed also later in the text) is that, in the limit of weak excitation (i.e., weak population of the upper level), the simulated temporal profile of the emission (supposed to be driven by spontaneous emission) is not entirely decreasing exponentially.

III. SIMULATION RESULTS

A numerical code based on the model described above has been built. The *active* materials considered in this article are K-shell photoionized magnesium (Secs. III A–III D) or nickel (Sec. III E). In magnesium, according to the level scheme depicted in Fig. 1, level 2 stands for $1s\ 2s^2\ 2p^6\ [3s^2]$ and level 1 stands for $1s^2\ 2s^2\ 2p^5\ [3s^2]$. In nickel, level 2 stands for $1s\ 2s^2\ 2p_{1/2}^2 2p_{3/2}^4\ 3s^2 3p^6 3d^8\ [4s^2]$ and level 1 stands for $1s^2\ 2s^2\ 2p_{1/2}^2 2p_{3/2}^3\ 3s^2 3p^6 3d^8\ [4s^2]$. Compared with neutral atoms, outer electrons in solid Mg or Ni (denoted by [...]) are delocalized. In what follows we either set populations 2 and 1 (likewise, the density of inversion) (Secs. III B and III C) or we explicitly consider a time-dependent pumping (Secs. III D and III E).

In this last case, initial atoms (in the state $|0\rangle \equiv 1s^2\ 2s^2\ 2p^6\ [3s^2]$ for Mg or $[Ar]3d^8\ [4s^2]$ for Ni) are photoionized by an external x-ray source (supposedly an XFEL beam), hereafter named as "the pump," tuned above the K edge. This pumping results in the population of the core-excited state $|2\rangle$ radiatively coupled to state $|1\rangle$ by the decay $2p \to 1s$. In conditions of weak pumping, this coupling corresponds to the usual $K\alpha$ fluorescence. Note that in conditions of weak pumping, state $|2\rangle$ predominantly decays via Auger decay (with the rate Γ_2), while both states $|1,2\rangle$ are also affected by the photoionizing pump. In Mg we neglect the fine-structure splitting of the $K\alpha$ line, since it is smaller than the Auger width. For Ni, the splitting $K\alpha_1 - K\alpha_2$ largely exceeds the Auger width, and we chose to consider the $K\alpha_1$ line only. Levels $|1,2\rangle$ are the two levels considered in our Maxwell-Bloch modeling. According to Figs. 1 and 2, quantities γ_1, γ_2, and X_p depend on the local intensity of the pump I_p in the sense that

$$\gamma_1(z,t) = \sigma_{1s}\frac{I_p(z,t)}{h\nu_p}, \tag{17}$$

$$\gamma_2(z,t) = \Gamma_2, \tag{18}$$

$$X_p(z,t) = \sigma_{1s}N_o(z,t)\frac{I_p(z,t)}{h\nu_p}, \tag{19}$$

where σ_{1s} denotes the $1s$ photoionization cross section at energy $h\nu_p$. I_p, $h\nu_p$ are the intensity (here a power per surface unit) and the photon energy of the pump, respectively. N_o is the population density of state $|0\rangle$. If $h\nu_p$ is greater than the second $1s$ ionization threshold, the term $\frac{\sigma_{1s}}{2}\frac{I_p(z,t)}{h\nu_p}$ must be added to the right side of Eq. (18). At this step it is important to remark that, for a normal incidence and being off an accidental situation where the period of the material would be an integer of $\lambda/2$ (i.e., off-Bragg), one may adopt for the pump the simple *corpuscular* point of view of photon absorption. Hence for a pump propagating from the right (see Fig. 2), the pump intensity obeys the following photon transport equation:

$$\frac{1}{c}\frac{\partial I_p(z,t)}{\partial t} - \frac{\partial I_p(z,t)}{\partial z} = -k_p(z,t)\, I_p(z,t), \tag{20}$$

with

$$\begin{aligned} k_p(z,t) &= \sigma_{1s}N_o(z,t) + \sigma_{1s}N_1(z,t) \\ &\quad + \frac{\sigma_{1s}}{2}N_2(z,t)\ \text{(in the active material)} \\ &= \sigma^{\text{passive}}N^{\text{passive}}(z,t)\ \text{(in the passive material)}, \end{aligned}$$

in which $N^{\text{passive}}(z,t)$ is the atom density in a *passive* layer, σ^{passive} being the corresponding absorption cross section at $h\nu_p$. Finally, the population of state $|0\rangle$ evolves as

$$\frac{\partial N_o(z,t)}{\partial t} = -\sigma_{1s} N_o(z,t) \frac{I_p(z,t)}{h\nu_p}. \tag{21}$$

In the case where the pump is explicitly taken into account, Eqs. (17)–(21) have to be solved simultaneously with the previous Maxwell-Bloch set of equations.

In the following, after checking the right behavior of the FDTD implementation (Sec. III A), we describe the propagation of an x-ray pulse at the $K\alpha$ energy for different situations of increasing complexity, whether the pulse is of external origin (Sec. III B) or not (i.e., originating from spontaneous emission, Secs. III C–III E). Note that in Secs. III D and III E we explicitly consider the pumping by an external photoionizing x-ray source.

A. Simple propagation in a multilayer material

A first and minimal implementation amounts to considering that all the layers are of *passive* nature, i.e., simply described by a complex refractive index. The goal is to assess the necessary number of subdivisions of each layer in our specific problem of wave propagation in the x-ray range, in a stratified medium made of nanometer-size layers. Indeed, this number of subdivisions defines a typical space interval Δz on which Maxwell equations are discretized according to the FDTD scheme mentioned above. Of course, this defines the time step Δt as discussed in Sec. II B. As a test case, we consider here a sample already considered in a context of synchrotron irradiation [26]. It consists of a stack of 30 bilayers (Mg/Co) of thicknesses $e_1 = 5.45$ nm and $e_2 = 2.55$ nm, respectively, so that the whole stack is denoted $(\text{Mg/Co})_{30}$. In each of the Mg layers, a source of radiation is supposed to emit at the $K\alpha$ line energy (1253.6 eV). These sources are all the same and of the form $E(t) = A \exp[-0.5(t-t_o)^2/\tau_p^2] \sin \omega_o t$ (where A is an arbitrary amplitude), implemented as discussed in Sec. II C. The resulting time-integrated outgoing emission over a time well exceeding both the time duration of the source and the time of propagation through the sample is displayed in Fig. 3 as a function of the number of subdivisions in each layer. Specific modulations (called Kossel patterns) are observed at the Bragg angles of the multilayer. These modulations are due to interferences of the diffracted waves inside the material [27,28]. Outgoing signals displayed in Fig. 3 are similar to those calculated for the same sample but by solving the Helmholtz wave equation for a plane-wave *incident* in the sample [14], which is just a check of the *optical reciprocity theorem* stated as *a point source at A will produce at B the same effect as a point of equal intensity placed at B will produce at A* [29,30]. Here, point A is a source point in the material while point B is a detection point at infinity. Now, one can consider the opposite point of view of a plane wave originating from B and incident on the material and calculate the electric field in the material (supposedly an N-cell stack). The resulting intensity (i.e., the sum of all of the local intensities) is equivalent to the total outgoing emission from N identical sources located in the N cells of the material.

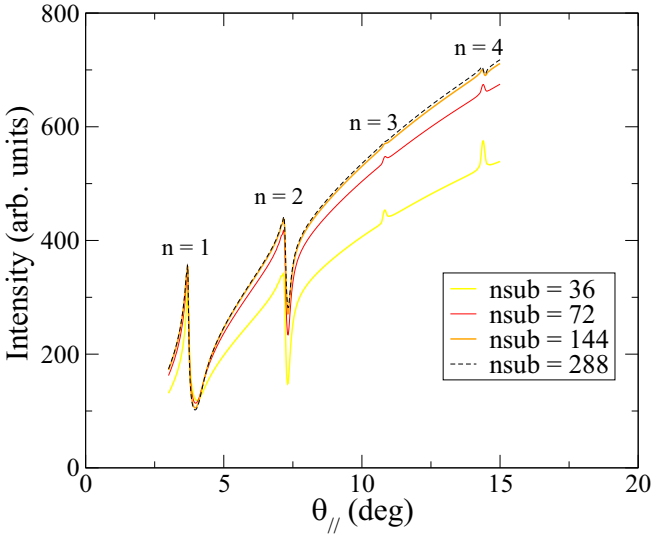

FIG. 3. Calculated angular scan for the Mg $K\alpha$ radiation emitted by a stack $(\text{Mg/Co})_{30}$ ($e_1 = 5.45$ nm and $e_2 = 2.55$ nm) where a same source of $K\alpha$ radiation has been put in each Mg layer. Kossel patterns are labeled by their Bragg order n.

In Fig. 3, one sees a convergence in the number of subdivisions necessary for performing accurate FDTD calculations of x-ray pulse propagation in multilayered materials. It is interesting to note the extinction of Kossel structure $n = 3$ for the converged results. This is consistent with the diffraction theory when applied to a simple line grating [30] or to X-UV interference mirrors [31]. Indeed, the first extinction should occur for the ratio $\frac{\Lambda}{e_2} = 3$. Taking for e_2 and for the period $\Lambda = e_1 + e_2$, the values given above, one finds a value very close to 3. These different remarks validate our minimal implementation.

B. Propagation in an amplifying multilayer material

We consider here the problem of a short pulse originating at the left, i.e., in the vacuum cell of our computational domain (see Sec. II B) and then propagating from left to right in a multilayer similar to the stack considered in the previous paragraph, albeit with an increased number of bilayers, i.e., $(\text{Mg/Co})_{60}$. The Mg layers are now *active*, i.e., described by the Bloch equations, and we consider four typical sets of initial populations for N_1, N_2 in term of the total density of atoms in solid state Mg, that is, $n_{\text{Mg}} = 4.3063 \times 10^{22}$ cm^{-3}. The population of the lowest level is fixed to $N_1 = 4.306 \times 10^{18}$ cm^{-3}, while N_2 is varied between 4.306×10^{17} cm^{-3} (case 1), 4.306×10^{20} cm^{-3} (case 2), 4.306×10^{21} cm^{-3} (case 3), 4.306×10^{22} cm^{-3} (case 4), respectively. In this way, case 1 corresponds to a very weak 1s photoionization with no inversion, while case 4 corresponds to a maximal population inversion in the Mg layers. The ingoing pulse is of the form $E(t) = \frac{1}{\sqrt{2\pi}\tau_p} \exp[-0.5(t-t_o)^2/\tau_p^2] \sin \omega_o t$ with the typical parameters $\tau_p = 1$ fs and $t_o = 2$ fs. What is specifically studied here is the right outgoing intensity as a function of time. More precisely, one displays the modulus of the Poynting vector, averaged over one period, i.e., $S_{av} = \frac{1}{T}\int_0^T |S| dt$ with $\mu_o^2 S^2 = (E_x B_z)^2 + (E_x B_y)^2$, $B_z = \frac{1}{c} E_x \sin\theta_\perp$. Hereafter,

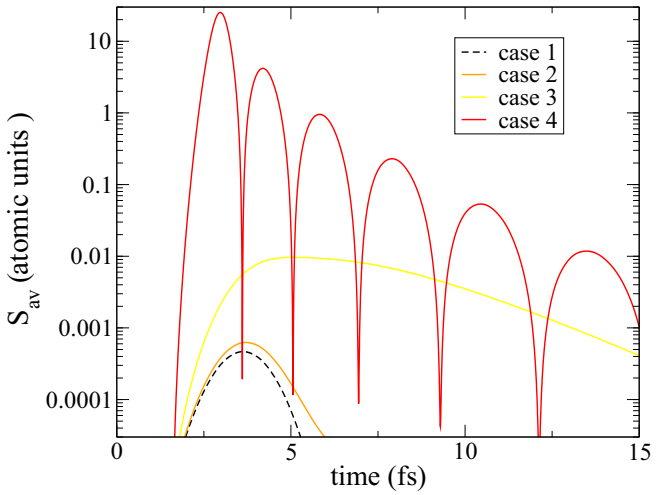

FIG. 4. Modulus of the Poynting vector outgoing from the stack $(Mg/Co)_{60}$ in the normal direction ($\theta_{//} = 90°$) as a function of time. See text for the characteristics of the ingoing signal and for the definition of cases 1–4.

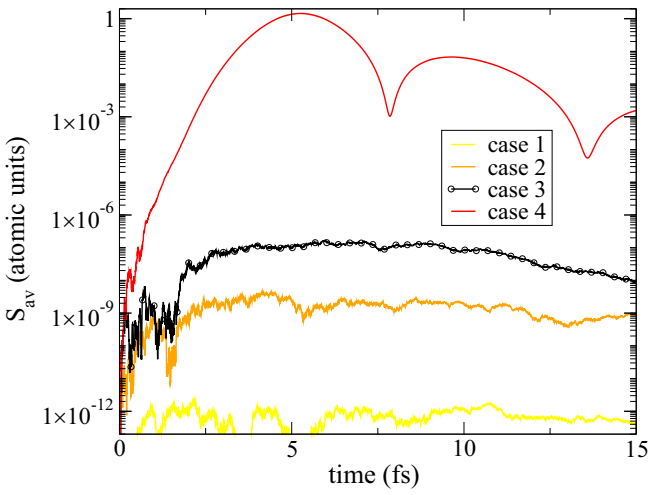

FIG. 6. Modulus of the Poynting vector outgoing from the stack $(Mg/Co)_{60}$ in the normal direction ($\theta_{//} = 90°$) as a function of time. The seeding is provided by the inherent spontaneous emission noise. See text for the for the definition of cases 1–4.

units for the Poynting vector are the atomic units, i.e.,S_{av} is in unit of $\frac{e^{12}}{(4\pi\epsilon_o)^6}\frac{m_e^4}{\hbar^9}$. For a signal ingoing in the normal direction, calculations are displayed in Fig. 4.

Compared with the weak signal (case 1), one sees the gradual effect of a gain material on the intensity temporal shape of the outgoing pulse. In particular, one notices an increase of the outgoing pulse duration with respect to the ingoing pulse duration. In the case of strong (and here maximal) inversion (case 4), a typical effect such as "ringing" of the outgoing signal is observed. This corresponds to the well-known Burnham-Chiao ringing [32]. Present simulations are in the time domain. Of course, taking the Fourier transform gives information on the frequency domain. Figure 5 shows the spectra corresponding to the previous simulations, i.e., the evolution of the (normalized) spectrum as a function of the density of inversion. Even on this small distance of propagation, the high density allows a clear gain narrowing

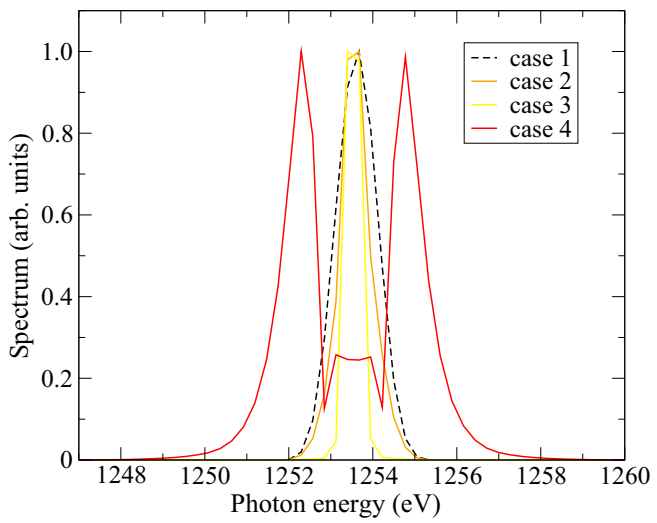

FIG. 5. Normalized spectra corresponding to the signals of Fig. 4.

(cases 2 and 3) and then a strong AC Stark (or Rabi) splitting for the maximal density of inversion (case 4). This behavior illustrates the response of the two-level system driven by an x-ray field on resonance. This field becomes so important that the levels shift dynamically through the Stark effect.

C. Self-emission of an amplifying multilayer material

In this paragraph we do not consider the propagation of an external pulse but the signal originating from the noisy source of spontaneous emission in each active cell of a multilayer. More precisely, we study how spontaneous emission emitted in one direction propagates and how stimulated emission sets in. Present calculations rely on the modeling of spontaneous emission presented in Sec. II C. Still, for the same multilayer $(Mg/Co)_{60}$ and the same sets of initial populations (N_1, N_2) in Mg layers, Fig. 6 displays simulations of the outgoing x-ray emission in the normal direction.

We see the weak noisy signal for a low initial excitation (case 1) while, gradually with the density of inversion, a collective emission is set up independently of any external pulse ingoing into the material. For the maximal initial population inversion (case 4), characteristics of the superradiance, namely, time delay for the peak of emission and ringing, are clearly visible. We emphasize that these results are just single realizations which may be subjected to large fluctuations. However, what we observed is that in case of strong population inversion, stimulated emission and amplification make the results weakly sensitive to a given realization, a fact which is somehow reflected by the smooth aspect of graph corresponding to case 4. In case of weak or absent stimulated emission, the right temporal behavior can be recovered only by performing an average over many realizations. For cases 1 and 2, we checked that an average over at least a few tens of realizations gives a decaying behavior for large time. Furthermore, in this weak limit we observed a behavior as $te^{-\Gamma t}$ (Γ being the decay time of level 2) instead of the right behavior $e^{-\Gamma t}$, which is an identified shortcoming of MB models with

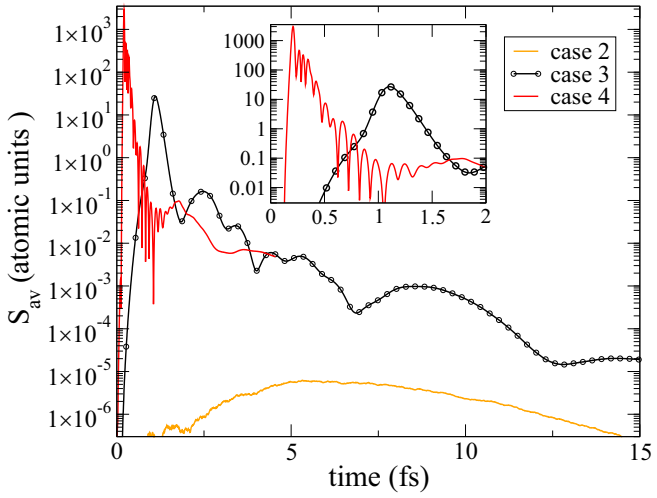

FIG. 7. Modulus of the Poynting vector outgoing from the stack $(Mg/Co)_{60}$ in first Bragg direction $\theta_{//} = 3.45$ deg as a function of time. The seeding is provided by the inherent spontaneous emission noise. See text for the for the definition of cases 2–4. The inset is a zoom of the time interval 0–2 fs.

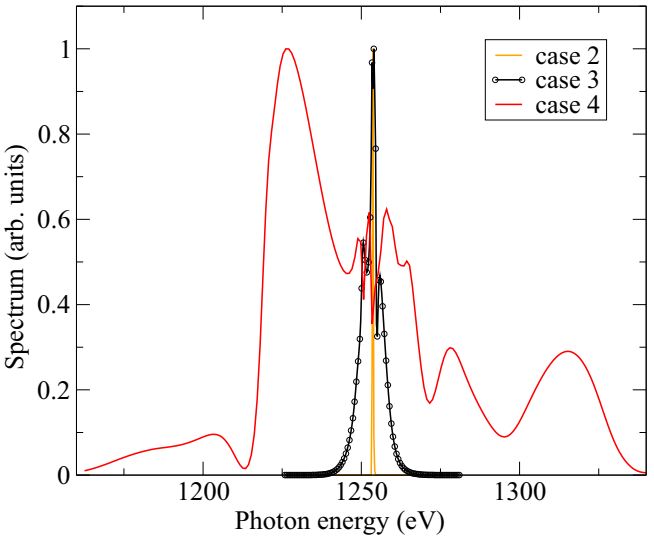

FIG. 8. Normalized spectra corresponding to the signals of Fig. 7.

a noise term [33,34]. In the weak limit, the present theoretical approach is thus not very reliable.

We turn now (Fig. 7) to a propagation seeded around the first uncorrected Bragg angle (defined so that $\Lambda \sin\theta_{//} = \lambda/2$, Λ being the period of the material, i.e., $\Lambda = e_1 + e_2$ according to Fig. 2). Here an oscillation feedback can be provided by Bragg reflection [12,13,35] so that large electric field enhancements can be obtained [14]. Note that for a multilayer and in the linear response regime, a small deviation to the previous Bragg law exists [31,36,37]. Compared with Fig. 6 (normal direction), a dramatic change of the emission is observed for $\theta_{//} = 3.45°$. Here at oblique incidence, the phase front of a plane-wave incident on the left is supposed to arrive on the opposite side in a very short time. This time τ is defined so that $c\tau = d \sin\theta_{//}$, d being the whole thickness of the multilayer, i.e., $\tau \simeq 0.1$ fs in present conditions. As one can see, depending on the inversion density, the outgoing x-ray pulse shifts earlier in time; its duration is reduced while its intensity strongly increases. This is a clear evidence of the feedback provided by Bragg reflection in the multilayer. Some complex "ringing" is also apparent. Here, also, we observed that stimulated emission, amplification, and feedback make the results weakly sensitive to a particular realization, which means that the random onset of emission is easily forgotten. Spectra corresponding to Fig. 7 are displayed in Fig. 8. The huge broadening observed for the maximal density of inversion (case 4) is a combined effect of the pulse shortening and of AC Stark splitting due to the huge electric field which sets up. These results suggest that for large population inversions, emission will tend to be around the Bragg angle and that its duration should be extremely short, beating even Auger decay, which is of the order of 2–3 fs.

At this step, it is important to comment the choice of the relative thicknesses which can be done to optimize the feedback. For our purpose, optimization of the multilayer relies on its intrinsic reflectivity at the wavelength of interest (i.e., here the $K\alpha$ line of active layers), regardless of any MB calculation. Relative thicknesses are thus important. A characteristic parameter is the ratio (usually called γ) of the heaviest layer (and more absorbing) thickness e_2 to the period. It is well known from multilayer physics that an optimal diffraction may be found for γ close to $1/3$. Using equations based on two different methods (either the dynamical theory of diffraction [38] as applied to multilayer optics [39]) or the "optical approach" as applied to multilayer optics [31], we have found that for the system (Mg/Co) the optimal γ is close to 0.4. So the rule of thumb of $\gamma \sim 1/3$ is verified and has been used as a typical value. Concerning the effect of possible imperfections in the periodicity, one can also look at the intrinsic reflectivity and see how it is sensitive to a small random variation of thicknesses. Considering 1% variation (which is a high limit from an experimental point of view) we have found that the reflectivity moves only 1%. Therefore small random variations of the thicknesses are not very important.

D. Self-emission of a pumped multilayer material

Previous calculations were based on the idea of a preliminary preparation of N_1, N_2 at given initial values. Here we place ourselves in conditions where these initial values are zero and where pumping of level 2 is provided by an external x-ray source photoionizing the ground level (of population N_0) within an active layer, as discussed at the beginning of Sec. III. This raises the question of the optimal size of the multilayer, i.e., of the number of bilayers. The answer depends on the material, on the attenuation length of the pump, and on the incidence angle. For a not too inhomogeneous pumping, the size of the multilayer for a given incidence angle cannot exceed the attenuation length of the pump.

In present simulations, the x-ray pulse is supposed Gaussian and of 10-fs duration (FWHM) and at normal incidence, i.e., according to Fig. 2. Its intensity is propagated and depleted according to Eq. (20). The photon energy of this pump is 1332 eV, i.e., above the Mg K edge. In Fig. 9 we plot the outgoing Mg $K\alpha$ emission of our $(Mg/Co)_{60}$ stack in

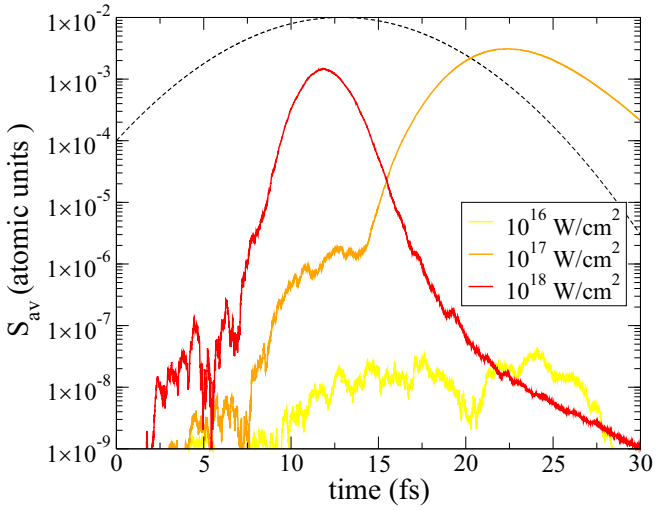

FIG. 9. Modulus of the Poynting vector outgoing from the stack $(Mg/Co)_{60}$ in the normal direction ($\theta_{//} = 90°$) as a function of time and for different intensities of an external x-ray pump. Dashes (of arbitrary unit) indicate the temporal shape of the pump. The seeding of the emission is provided by the inherent spontaneous emission noise.

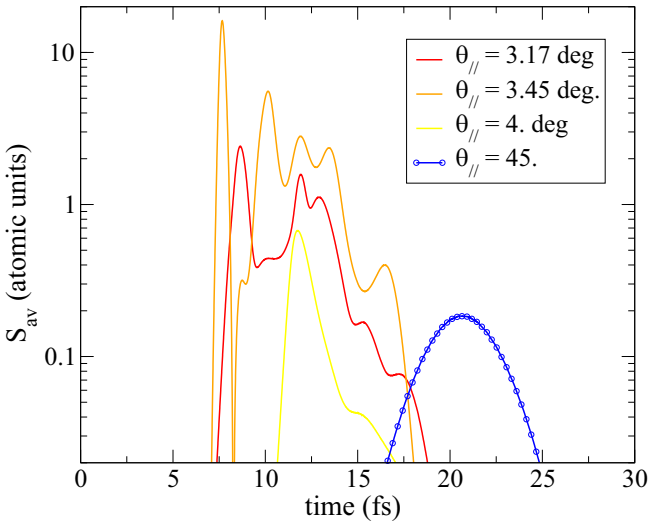

FIG. 11. Modulus of the Poynting vector outgoing from the stack $(Mg/Co)_{60}$ in four directions as a function of time and for the intensity 10^{17} W/cm^2 (of external x-ray pump). The seeding of the emission is provided by the inherent spontaneous emission noise.

the normal direction as resulting from three different pump intensities. Dashes (of arbitrary unit) indicate the temporal shape of the pump. Here the different shapes of the outgoing emission reflect the efficiency of the core-hole creation with respect to the maximum of intensity. As seen above, the signal stops being noisy when stimulated emission sets up, which is possible if a sufficient density of core holes is reached. Now, as expected from the considerations of Sec. III C, the signals observed in the Bragg direction $\theta_{//} = 3.45°$, are dramatically different (Fig. 10), both in intensity (a few orders of magnitudes) and in temporal shape. About the different angles of emission, a question arises here. In principle, spontaneous

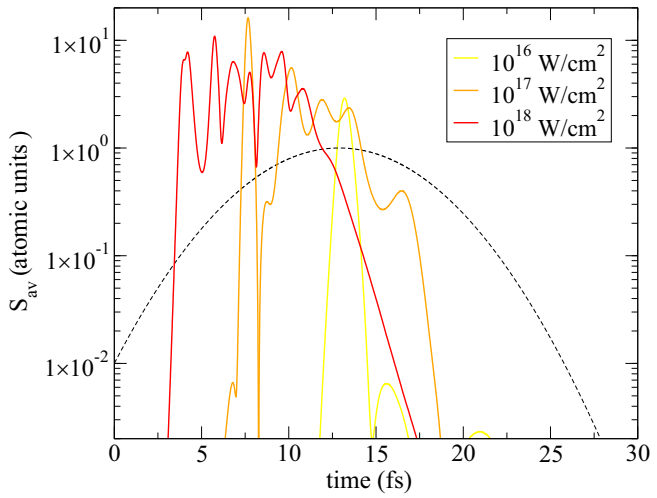

FIG. 10. Modulus of the Poynting vector outgoing from the stack $(Mg/Co)_{60}$ in the direction $\theta_{//} = 3.45°$ as a function of time and for different intensities of the external x-ray pump. Dashes (of arbitrary unit) indicate the temporal shape of the pump. The seeding of the emission is provided by the inherent spontaneous emission noise.

emission (which is isotropic) generates photons in all directions, although at different times and different locations. For this reason the fields corresponding to all directions should be calculated so that Eqs. (4)–(6) include the contribution of all directions. In terms of computation time, such a treatment is prohibitive since, as discussed in Sec. III A and seen in Fig. 3, a very fine spatial zoning and a very fine angular gridding is needed to resolve the Kossel structures. Here our purpose is to show that a multilayer structure may present preferential directions of emission for which initial photons emitted around the Bragg angle "catch on" the stimulated emission as does a standard cavity. This point is illustrated in Fig. 11, which, for the same multilayer and for the intensity 10^{17} W/cm^2, displays at $\theta_{//} = 45°$ and for three angles at and around the Bragg angle, the temporal profiles of radiation. What is shown in this figure is twofold. First, one sees that most of the emission is catch on around the Bragg angle $\theta_{//} = 3.45°$. Second, it is clear that the enhancement of the emission is not a simple geometry effect where this enhancement would come from a larger effective propagation distance.

In Fig. 10, the complex behavior of outgoing signals reflects the complex interplay between population kinetics, depletion of the pump, propagation, and Bragg diffraction. This is somehow illustrated by snapshots of the spatial distribution (inside the multilayer) of populations N_0, N_1, N_2 at different characteristic times during the driving pump pulse (Fig. 12). The x-ray pump comes on the right so that the decrease of population N_0 as a function of z reflects the attenuation of the pump as it propagates from the right to the left inside the material. The Maxwell-Bloch coupling of populations N_2, N_1, seeded by spontaneous emission, gives rise to a set of pulses propagating inside the multilayer and to clear Rabi oscillations (Rabi flopping). Despite the complex temporal shape of these outgoing signals around the Bragg direction, they remain much more intense than in the normal direction.

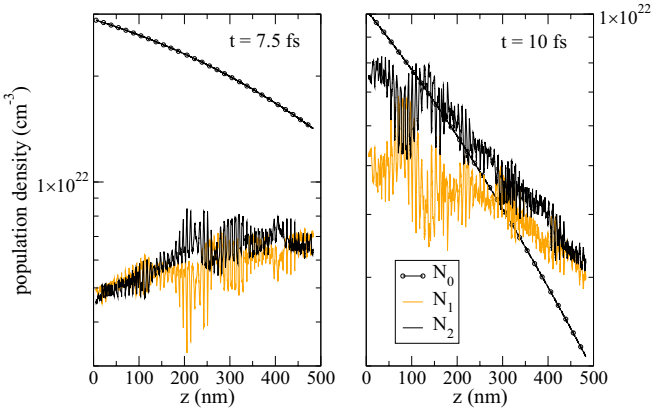

FIG. 12. Snapshots of populations N_0, N_1, N_2 at two moments inside the multilayer $(Mg/Co)_{60}$ and in the conditions of Fig. 10. The pump comes on the right with an intensity of 10^{18} W/cm^2. Left figure: $t = 7.5$ fs; right figure $t = 10$ fs.

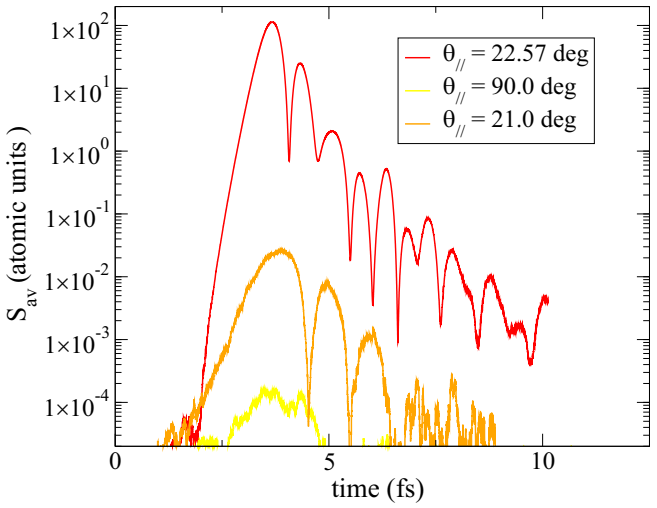

FIG. 13. Modulus of the Poynting vector outgoing from the stack $(Ni/vacuum)_{5000}$ ($e_1 = 0.0972$ nm, $e_2 = 0.1188$ nm) irradiated in the normal direction by a raised cosine pulse of intensity 10^{19} W/cm^2, 10 fs duration, 8360 eV photon energy. Three outgoing directions are shown: the normal direction $\theta_{//} = 90°$, the Bragg direction $\theta_{//} = 22.57°$, and an off-Bragg axis direction $\theta_{//} = 21.0°$. Seeding of the emission is provided by the inherent spontaneous emission noise.

As massive photoionization causes a large concentration of photoelectrons which thermalize quickly in dense materials, an interesting question is to what extent collisional ionization of $2p$ electrons in level 2 by these photoelectrons may affect significantly the lifetime of this level. Assuming an instantaneous thermalization, a temperature for these photoelectrons can be estimated from the total energy deposited in these photoelectrons. In Mg and with our parameters, we estimated this electron temperature to be of the order of 100 eV for a pump intensity of 10^{18} W/cm^2. From a calculation of the collisional ionization cross section of a $2p$ electron in state $1s\ 2s^2\ 2p^6\ [3s^2]$, the collisional ionization rate varies between 10^9 s^{-1} (at 10 eV) and 10^{14} s^{-1} (at 100 eV). This can be compared with the autoionization rate which is 3.4×10^{14} s^{-1}. Although not negligible at high intensity, still, at the end of the pump pulse, the effect of photoelectrons remains smaller than autoionization decay. We do not think that their existence changes the conclusions of this article, especially in the feedback regime, which shortens the emission duration.

E. Self-emission of a pumped natural crystal

In this last section we examine the case of a natural crystal whose periodicity of atomic layers may provide the same kind of Bragg oscillations. One considers here a Ni crystal where for an orientation (111) of planes parallel to the surface, atomic layer spacing is $d = 0.216$ nm. A strong pumping of the $1s$ core electrons in Ni may give rise to an amplification on the $2p_{3/2} \rightarrow 1s\ K\alpha_1$ line at 7478.15 eV. At this energy the first Bragg angle is around 22.6° (with respect to the surface). 1D periodicity is introduced in the calculations by considering the (supposedly perfect) crystal as a stack of bilayers of period d and where the first layer (the active layer) is a layer of Ni atoms while the second layer is just empty (then passive) and of refractive index 1. Such a replacement of real atoms by a uniform layer of a given thickness e_1 (see Fig. 2) is a rough method to simulate the problem of a distribution of individual small scatterers. Its validity is semiempirical. A relevant quantity to measure its effectiveness is the reflectivity of the system $(element/vacuum)_n$, which for a wavelength of interest can be calculated around the Bragg angle and compared with a model giving the reflectivity of a real crystal. From x-ray reflectivity calculations based on a solution of the Helmholtz equation applied to stacks $(element/vacuum)_n$, we performed such comparisons with a software available at Stepanov's x-ray server [40], allowing a calculation of the reflectivity in real crystals. We found that taking for the element thickness a typical value of $0.4d$ (d being the proper inter-reticular distance in the crystal of interest) and renormalizing properly the number of atoms in this element layer to the right number of atoms (per volume unit), this approach gives results close to those of Stepanov's x-ray server. Accordingly, we used this recipe in our Maxwell-Bloch calculations.

Simulations presented here correspond to a Ni thickness of 1.08 μm, i.e., to the stack $(Ni/vacuum)_{5000}$. Simulation results are displayed in Fig. 13. Irradiation conditions are a raised cosine pulse of 10-fs duration (FWHM), 8360 eV of photon energy (i.e., above the Ni K edge) and of intensities 10^{19} W/cm^2, and at normal incidence, i.e., in the geometry of Fig. 2. Figure 13 displays a comparison of the outgoing Ni $K\alpha_1$ signal (i.e., seeded by spontaneous emission) observed in the normal direction $\theta_{//} = 90°$, in the Bragg direction $\theta_{//} = 21.57°$, and in some off-Bragg direction, respectively. Compared with the other directions, emission in the Bragg diffraction region (the Kossel region) is strongly enhanced, which indicates the possibility of having a resonator or feedback effect in natural crystals.

IV. CONCLUSION

A 1D Maxwell-Bloch FDTD model for any oblique incidence has been successfully implemented for studying x-ray propagation in 1D photonic crystals. We simulated the self-emitted signal from typical 1D photonic crystals where

a population inversion is prepared on an atomic transition in the x-ray range. The buildup of an outgoing signal starts from spontaneous emission. We have seen that this emission encompasses many nonlinear phenomena such as Rabi splitting, Rabi flopping, ringing, etc., in the x-ray range as well as the Kossel effect, but in an *amplified mode*. We have shown that most of the emission occurs in a prevailing direction which is the Bragg direction. If the inversion results from a previous photoionization, we observed that this emission is short enough to beat Auger relaxation. We specifically studied cases where the pumping source allowing a strong population inversion is an intense, short x-ray pulse such as provided by XFEL sources. For a typical multilayer and for realistic conditions of pumping, calculations show a strong enhancement of the emission in the Bragg direction. For the case of natural crystals, this enhancement is also noticeable.

Results of this study motivate future experimental investigations of the behavior of photonic crystals, whether they are natural or artificial (multilayers). It motivates also many other theoretical investigations on different multilayers or natural crystals to optimize x-ray emission at different wavelengths.

ACKNOWLEDGMENTS

At numerous times during the course of this work, one of us (O.P.) has benefited from discussions and helpful advice concerning the use of computational resources from Paul Genesio at PIIM Laboratory.

[1] B.W. Adams *et al.*, J. Mod. Opt. **60**, 2 (2013).
[2] B.W. Adams, *Nonlinear Optics, Quantum Optics and Ultrafast Phenomena with X-rays* (Kluwer Academic Publisher, Norwell, MA, 2008).
[3] Yu-Ping Sun, Ji-Cai Liu, Chuan-Kui Wang, and Faris Gel'mukhanov, Phys. Rev. A **81**, 013812 (2010).
[4] N. Rohringer *et al.*, Nature **481**, 488 (2012).
[5] A. Benediktovitch, L. Mercadier, O. Peyrusse, A. Przystawik, T. Laarmann, B. Langbehn, C. Bomme, B. Erk, J. Corréa, C. Mossé *et al.*, Phys. Rev. A **101**, 063412 (2020).
[6] M. Beye *et al.*, Nature (London) **501**, 191 (2013).
[7] H. Yoneda *et al.*, Nature (London) **524**, 446 (2015).
[8] P. Jonnard *et al.*, Struct. Dyn. **4**, 054306 (2017).
[9] T. Kroll, C. Weninger, R. Alonso-Mori, D. Sokaras, D. Zhu, L. Mercadier *et al.*, Phys. Rev. Lett. **120**, 133203 (2018).
[10] A. Halavanau *et al.*, Proc. Natl. Acad. Sci. USA **117**, 15511 (2020).
[11] M. Nagasono *et al.*, Phys. Rev. Lett. **107**, 193603 (2011).
[12] A. Yariv and P. Yeh, Opt. Commun. **22**, 5 (1977).
[13] J.-M. André, K. Le Guen, and P. Jonnard, Laser Phys. **24**, 085001 (2014).
[14] O. Peyrusse, P. Jonnard, K. LeGuen, and J.-M. André, Phys. Rev. A **101**, 013818 (2020).
[15] J.C. MacGillivray and M.S. Feld, Phys. Rev. A **14**, 1169 (1976).
[16] O. Larroche, D. Ros, A. Klisnick, A. Sureau, C. Moller, and H. Guennou, Phys. Rev. A **62**, 043815 (2000).
[17] Clemens Weninger and Nina Rohringer, Phys. Rev. A **90**, 063828 (2014).
[18] C. Lyu, S. M. Cavaletto, C. H. Keitel *et al.*, Sci. Rep. **10**, 9439 (2020).
[19] A. Taflove, *Computational Electrodynamics, The Finite-Difference Time-Domain Method* (Artech House, Boston, MA, 1995).
[20] B. L. Henke, E. M. Gullikson, and J. C. Davis, At. Data Nucl. Data Tables **54**, 181 (1993).
[21] CXRO http://www.cxro.lbl.gov/.
[22] M. O. Scully and M. S. Zubairy, *Quantum Optics* (Cambridge University Press, Cambridge, England, 1997).
[23] K.S. Yee, IEEE Trans. Antennas Propag. **14**, 302 (1966).
[24] B. Engquist and A. Majda, Math. Comput. **31**, 629 (1977).
[25] D. E. Merewether, R. Fisher, and F. W. Smith, IEEE Trans. Nucl. Sci. **27**, 1829 (1980).
[26] P. Jonnard *et al.*, J. Phys. B **47**, 165601 (2014).
[27] E. Langer and S. Däbritz, IOP Conf. Series: Mater. Sci. Eng. **7**, 012015 (2010).
[28] K. Le Guen *et al.*, J. Nanosci. Nanotechnol. **19**, 593 (2019).
[29] W. Schülke and D. Brümmer, Z. Naturforsch. A **17**, 208 (1962).
[30] M. Born and E. Wolf, *Principles of Optics*, 6th ed. (Pergamon Press, New York, 1980).
[31] B. Pardo, T. Megademini, and J. M. André, Rev. Phys. Appl. **23**, 1579 (1988).
[32] D. C. Burnham and R. Y. Chiao, Phys. Rev. **188**, 667 (1969).
[33] S. Krusic, K. Bucar, A. Mihelic, and M. Zitnik, Phys. Rev. A **98**, 013416 (2018).
[34] Andrei Benediktovitch, Vinay P. Majety, and Nina Rohringer, Phys. Rev. A **99**, 013839 (2019).
[35] A. Yariv, Appl. Phys. Lett. **25**, 105 (1974).
[36] D. Attwood, *Soft X-rays and Extreme Ultraviolet Radiation* (University of California, Berkeley, Berkeley, CA, 2007).
[37] C. T. Chantler and R. D. Deslattes, Rev. Sci. Instrum. **66**, 5123 (1995).
[38] B. W. Batterman and H. Coles, Rev. Mod. Phys. **36**, 681 (1964).
[39] I. V. Kozhevnikov and A. V. Vinogradov, Phys. Scr. **1987**, 137 (1987).
[40] Stepanov's x-ray server, https://x-server.gmca.aps.anl.gov.